AIAA JOURNAL
Vol. 48, No. 6, June 2010

Simulations of Vortex Formation Around a Blunt Wing Tip

Ali Uzun* and M. Yousuff Hussaini†
Florida State University, Tallahassee, Florida 32306-4510

DOI: 10.2514/1.J050147

We report our findings from a computational study on wing-tip vortices. The main emphasis of the simulations is to compute the formation of a tip vortex around a blunt wing tip and its interaction with the wing and tip side-edge surfaces. Comparisons of simulation results with available experimental data are done to assess the prediction capability of the simulations. The simulations are performed on a computational grid containing 110 million points total. The blunt tip geometry actually gives rise to the formation of two vortices. The primary vortex forms over the upper surface of the wing, and the secondary vortex forms off of the side edge. These two vortices merge together around the tip trailing edge to form the tip vortex. Simulations at the experimental Reynolds number of 1.8×10^6 are performed using several subgrid-scale models. It is shown that the simulation performed without an explicit subgrid-scale model, also known as implicit large eddy simulation, produces the best agreement with the experimental measurements. Although some differences between the simulation results and experimental data still exist, the overall agreement between the experiment and simulation is found to be satisfactory.

Nomenclature

a	=	speed of sound
b	=	wing span
C_p	=	pressure coefficient $(p - p_\infty)/\frac{1}{2}\rho u_\infty^2$
c	=	wing chord length
f	=	frequency
p	=	static pressure
Re_c	=	wing chord Reynolds number, $\rho_\infty u_\infty c/\mu_\infty$
u_τ	=	wall friction velocity, $\sqrt{\tau_{\text{wall}}/\rho}$
u, v, w	=	Cartesian velocity components in x, y, and z directions
x, y, z	=	Cartesian coordinates in streamwise, vertical, and spanwise directions
ΔW_n	=	wall-normal grid spacing
Δt	=	time increment
μ	=	molecular viscosity
ρ	=	fluid density
τ_{wall}	=	wall shear stress
∞	=	freestream value

Superscript

$+$	=	value given in wall units

I. Introduction

STRICT regulations on aircraft noise have made it necessary to significantly reduce both the propulsion system noise and airframe noise for future aircraft. Although jet exhaust noise is the most important component of propulsion system noise, airframe noise consists of several equally important components, such as flap side-edge noise (tip vortex noise), trailing-edge noise, slat-cove noise, jet–flap-interaction noise, and landing gear noise. Further reduction of airframe noise requires a good understanding of these different components so that appropriate noise-reduction technologies can be developed accordingly.

Tip vortex noise is a problem that is commonly encountered with the airflow around flap side edges of high-lift systems found in aeronautical applications. Because of the pressure differences between the suction and pressure sides of the wing tip (or the flap tip), a crossflow over the side edge of the tip occurs and gives rise to the formation of a tip vortex. The interaction of the tip vortex with the side edge and the trailing edge of the tip results in the so-called tip noise. Tip vortices can be an important source of airframe noise, especially during aircraft landing, when the engines are operated at a low power setting and much of the noise originates from the high-lift systems that are deployed for landing. Control and minimization of tip vortex noise are important for the future design of aircraft high-lift systems and other applications such as quieter wind turbine blade tips that could benefit from such technological advances. Tip vortex noise is an important problem for wind turbine blades as well, and the desire for further reduction of noise levels in the vicinity of wind turbine farms provides additional motivation for the study of this problem. Even without its noise aspect, the tip vortex is still important because it plays a significant role in other problems such as the landing separation distance for aircraft and the vibration caused by blade–vortex interaction on helicopter blades. Thus, a better understanding of the tip vortex problem is necessary in order to mitigate its undesirable side effects (such as noise, vibration, landing distance separation, etc.) in various applications.

Although experiments are essential and provide useful data, they can supply only a limited amount of information. Properly validated computational techniques, on the other hand, have the potential to provide much more detail about the problem of interest. Recent improvements in the processing speed of computers have indeed made numerical techniques quite useful and popular in the study of various aerodynamics and aeroacoustics problems of interest. For example, regarding the tip vortex problem, the studies of Dacles-Mariani et al. [1,2] as well as that of Kim and Rhee [3] have used Reynolds-averaged Navier–Stokes (RANS)-type simulations to study the mean flowfield of the vortex around the rounded tip of a NACA0012 wing with good success. Takallu and Laflin [4] as well as Khorrami et al. [5] have also used RANS calculations to study the tip vortex formation around flap side edges in high-lift systems. However, if the goal is to predict noise, then the use of RANS for noise prediction becomes questionable, because RANS methods heavily rely on turbulence models to model all of the relevant turbulence scales. Moreover, such methods try to predict the noise using the mean flow properties provided by a RANS solver. Since noise generation is a multiscale problem that involves a wide range of length and time scales, it appears that the success of RANS-based

Presented as Paper 2913 at the 14th AIAA/CEAS Aeroacoustics Conference, Vancouver, British Columbia, Canada, 5–7 May 2008; received 20 August 2009; revision received 16 October 2009; accepted for publication 9 November 2009.

*Research Associate, Program in Computational Science and Engineering. Senior Member AIAA.

†Sir James Lighthill Professor, Program in Computational Science and Engineering; Fellow AIAA.

noise-prediction methods will remain limited to specific cases for which semi-empirical noise models exist. One specific case in which RANS-based methods have been particularly successful is axisymmetric subsonic jet noise. Presently, there is no semi-empirical noise model available for tip vortex noise and, to our best knowledge, there has not been any attempt to compute the tip vortex noise using information from a RANS computation either.

Large eddy simulation (LES) techniques, although still computationally expensive, are becoming increasingly popular in computational aeroacoustics (CAA) research. The recent studies of Fleig et al. [6,7], Cai et al. [8], Ghias et al. [9], Imamura et al. [10,11], and Uzun et al. [12] are some of the first applications of LES to the tip vortex problem. The presence of large flow gradients within the boundary layer over the tip surface, as well as in the tip vortex vicinity and the near-field wake, requires sufficiently small grid spacings within these crucial regions so that the separation of the boundary layer followed by a rollup into a vortex and the complex vortex dynamics are accurately captured. The resulting computational grids needed in the LES of a tip vortex may easily reach a size that is on the order of tens of millions of points or even larger. Such substantial resolution requirements have perhaps stood in the way of expansive application of LES to the tip vortex problem.

To give the reader a sense of the grid resolution needed, Cai et al. [8] used a grid of 25 million points for the LES of a tip vortex around a NACA0012 wing geometry with a rounded tip, and the LES of Ghias et al. [9] used over 12 million grid points for the computation of the tip vortex around a NACA2415 wing geometry with a blunt tip. In our recent LES of a tip vortex on overset grids [12], we used 26.2 million grid points. Imamura et al. [10] initially used about 6 million grid points for the hybrid LES/RANS calculation of the flow and tip vortex around a rectangular NACA0012 wing with a blunt tip. They used 20 million points in a second calculation of the same problem [11]. In these hybrid calculations, they performed the LES only in the tip region and switched to RANS in the wing-root region. The switching between LES and RANS was done gradually by means of a linearly varying weight function. The LES studies of Fleig et al. [6,7] employed a grid consisting of 300 million grid points for the computation of the tip vortex and the flow around an entire wind turbine blade, even though their main goal was to only study the tip vortex noise. In contrast, the LES of Cai et al. [8], Ghias et al. [9], Imamura et al. [10,11], and Uzun et al. [12] consider the spanwise portion of the wing geometry that extends only several chord lengths from the tip region toward the root. Their approach appears to be more economical than that of Fleig et al. [6,7]. It should also be noted here that only the studies of Fleig et al. [6,7] and Imamura et al. [10,11] focus on the noise aspect of this problem, whereas the other LES studies are concerned with turbulence simulation only.

The application of LES to tip vortex noise prediction is still in its infancy and there is much room for growth. As a first step toward obtaining a high-quality numerical solution for a tip vortex, we have previously performed an LES of a wing-tip vortex around a rounded geometry using a multiblock LES code that is based on high-order schemes and that also has overset grid capability [12]. The sound field is typically several orders of magnitude smaller than the aerodynamic field, and compact finite difference schemes are known to satisfy the strict requirements of CAA while providing adequate wave resolution with typically less than 10 grid points per wavelength [13,14]. The high-order accuracy provided by compact schemes helps reduce the grid-resolution requirement and hence the overall computational cost.

It has been previously shown that the multiblock and overset capabilities of our LES code provide flexibility in meshing complex computational domains while allowing grid density control in various regions. High-order accurate schemes ensure a high-quality numerical solution, whereas implicit time-stepping brings great savings in computing cost. In addition to the simulation of tip vortex formation around a rounded tip [12], the same flow solver was also used in a round-jet simulation [15] and a chevron-jet simulation [16], demonstrating the applicability of the flow solver to different problems in turbulence and aeroacoustics.

In the present work, we simulate the tip vortex formation around a NACA0012 wing with a blunt tip for which there are some experimental measurements in the vicinity of the tip region [10]. Experimental measurements for this test case consist of particle image velocimetry (PIV) measurements of the mean velocity field and turbulent kinetic energy in the tip region and the spectra of the pressure fluctuations at certain points on the wing surface near the tip and on the tip side-edge surface. Although no far-field noise measurements have been taken in the experimental work, pressure fluctuations on the wing and tip side-edge surfaces are expected to carry a footprint of the far-field noise. This is because tip vortex noise is generated by the interaction of the tip vortex with the wing and tip side-edge surfaces. Thus, the correct prediction of the surface-pressure spectra can be a direct indicator of the far-field noise-prediction capability of a simulation method. Simulations results are compared with the available experimental data to assess the prediction capability of the simulations.

Imamura et al. [10,11] showed that although their hybrid RANS/LES approach produced good overall agreement between the computed and the experimentally measured tip vortex mean flow, the pressure fluctuation spectra taken at certain locations on the wing and tip side-edge surfaces displayed significant discrepancies compared with the experiment. This indicates that although the computational method they have used was able to capture the mean flow fairly well, the correct prediction of the unsteady characteristics of the tip vortex flow still needs additional work. As mentioned earlier, the correct prediction of the surface-pressure spectra can be a direct indicator of the far-field noise-prediction capability of a simulation method. In the present study, we make a more thorough comparison between the computed mean tip vortex flowfield and the experiment to validate our computations. Imamura et al. [10,11] only compared mean axial velocity and turbulent kinetic energy for the tip vortex mean flow, whereas we perform a comparison of mean crossflow velocity, mean crossflow streamlines, and mean axial-vorticity magnitude, in addition to mean axial velocity and turbulent kinetic energy. Through these comparisons, it is shown that the mean tip vortex flowfield is captured fairly well in our simulations. Moreover, it is shown that the overall agreement between our computed surface-pressure fluctuation spectra and the experimental spectra is better than that observed in the studies of Imamura et al. [10,11], thus providing additional credibility to the present simulation methodology.

II. Computational Methodology

For the sake of brevity, the details of our computational methodology are skipped here. The reader is referred to our previous publications [12,15,16] for the details of the simulation techniques. This section will only provide the details of the subgrid-scale (SGS) models that were used in our calculations.

The default SGS model employed in our LES code is the so-called implicit SGS model. The implicit SGS model relies on the numerical dissipation provided by the spatial filter. In other words, the spatial filter implemented in the LES for numerical stability is treated as an implicit SGS model. Thus, this approach belongs to the implicit LES (ILES) class of methods. It is well understood in turbulent flows that the energy cascade is associated with a mean flux of energy that is directed from large scales toward small scales. The large scales contain the major part of the turbulent kinetic energy and they continuously feed the turbulent kinetic energy via the cascade to the smallest eddies, where it is dissipated. Since the grid resolution in an LES is too coarse to resolve all of the relevant length scales, the pileup of energy at the high wave numbers can be eliminated through the use of a spatial filter. Hence, the spatial filter can be thought of as an effective SGS model in an LES. In support of this observation, Visbal and Rizzetta [17] and Visbal et al. [18] have performed LES of turbulent channel flow and compressible isotropic turbulence decay without using any explicit SGS model. In those simulations, they used high-order compact finite difference schemes and spatial filters similar to those we are using. Spatial filtering was treated as an implicit SGS model in their calculations. The ILES approach was found to produce acceptable results in the problems they studied.

They also showed that the use of an explicit SGS model in those simulations did not produce results superior to those obtained without employing an SGS model. The ILES approach has been successfully used by Sherer and Visbal [19] in turbulent channel-flow computations as well.

The first simulation we performed in this work employs the ILES approach. We also performed additional calculations using two explicit SGS models to investigate whether those explicit SGS models could improve the agreement between the computational results and the experimental data. One of the SGS models we tested is the so-called dynamic mixed model [20,21], which is a combination of the scale similarity [22,23] and the well-known dynamic Smagorinsky model. It is commonly argued that the scale-similarity model alone does not provide sufficient dissipation; thus, it is combined with the dynamic Smagorinsky model in this dynamic mixed model. The coefficient of the Smagorinsky model is computed as a function of space and time using a dynamic procedure. Dynamic computation of the Smagorinsky coefficient requires test filtering of certain quantities at a scale larger than the grid size, usually at twice the grid size. For this SGS model, we use the five-point optimized box filter developed by Sagaut and Grohens [24] for test filtering at a scale equal to twice the grid spacing.

We also tested another SGS model called the selective mixed-scale model [25,26]. This is another eddy-viscosity-type model. The length scale used in the model depends on both the small and large scales, and hence it is called the mixed-scale model. The eddy-viscosity is given by a nonlinear combination of Smagorinsky and mixing-length models. This is done in order to alleviate some of the well-known drawbacks of the Smagorinsky model. The selective function used in the model allows the eddy viscosity to go to zero in laminar, two-dimensional, and fully resolved regions. This function is based on the local angular fluctuation of the vorticity. There are several parameters that appear in the model. Values of these parameters were set to be constant and taken from the aforementioned references. In this SGS model, test filtering is only needed to compute the turbulent kinetic energy in the smallest resolved scales. For that purpose, we use a simple three-point box filter. More details on all of the subgrid-scale models we implemented can be found in the provided references.

III. Test Case: Vortex Formation Around a Blunt Tip

A. Simulation Details

We will present results from the simulations of an experimental test case previously studied by Imamura et al. [10]. The experimental setup is shown in Fig. 1. This test case studies the tip vortex formation around a wing with a blunt tip. The blunt tip geometry is a generic representation of a flap tip. Blunt tips can also be found in some wind turbine blades. The wing cross section has the NACA0012 airfoil geometry. The ratio of the wing span b to the chord c is 2.5. The model is mounted on the side wall of the wind-tunnel test section, as shown in the figure. The model is rotated about the quarter-chord axis to adjust the freestream angle of attack. All lengths are nondimensionalized by a reference length scale, which is taken as the constant wing chord length c. For the computational setup, the x direction is taken as the streamwise direction, y is the vertical direction, and z is the spanwise direction. The origin of the xyz coordinate system is attached to the quarter-chord location on the wing tip. Thus, $z/c = 0$ corresponds to the wing-tip plane. The wing-root plane is at $z/c = -2.5$. The freestream flow approaches the wing model at a Mach number of approximately 0.175 and an angle of attack of 12 deg. The Reynolds number, based on the freestream velocity, freestream kinematic viscosity, and wing chord length Re_c, is about 1.8×10^6 in the experiment.

It should be mentioned at this point that this is a fairly high, and thus a challenging, Reynolds number to simulate numerically. Since we have to work with limited computational resources, we set the

Fig. 1 Experimental setup (taken from [10,11]).

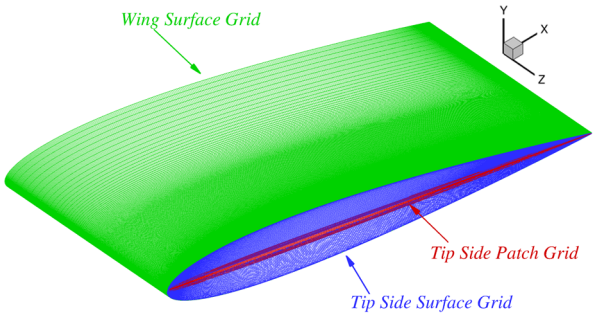

Fig. 2 Surface grids on the wing surface near the tip and on the tip side edge.

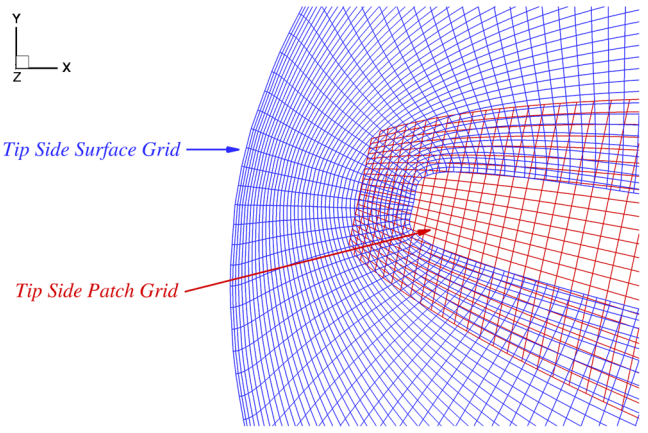

Fig. 3 Details of the grids near the tip leading edge.

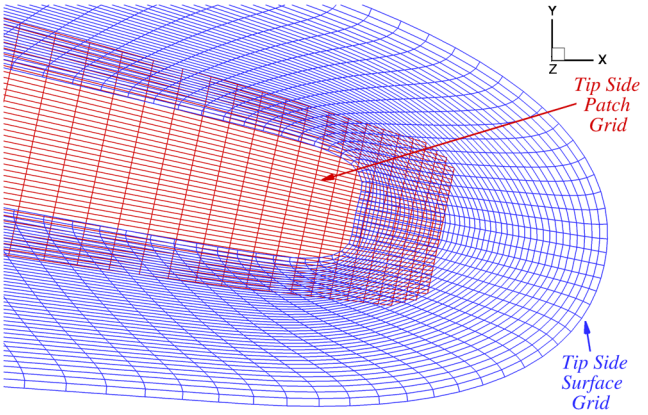

Fig. 4 Details of the grids near the tip trailing edge.

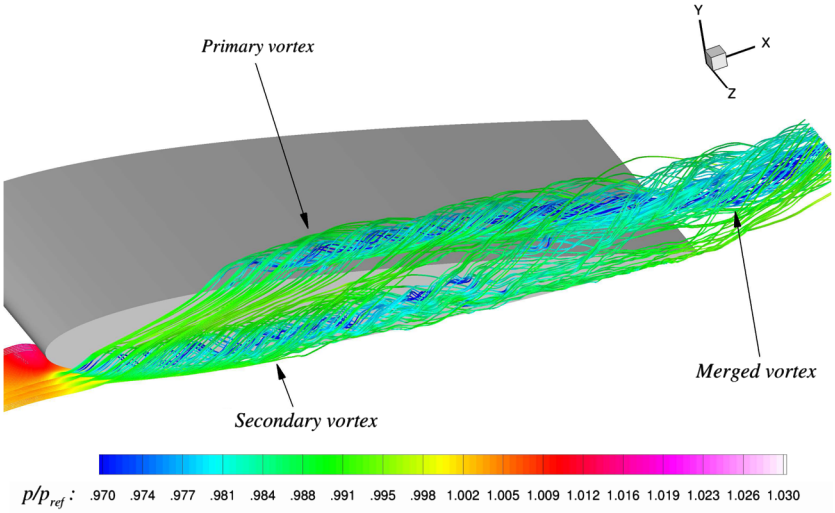

Fig. 5 Some streamlines depicting the formation of the primary vortex and the secondary vortex and their merging in simulation A. Colors denote the instantaneous value of pressure normalized by the freestream pressure.

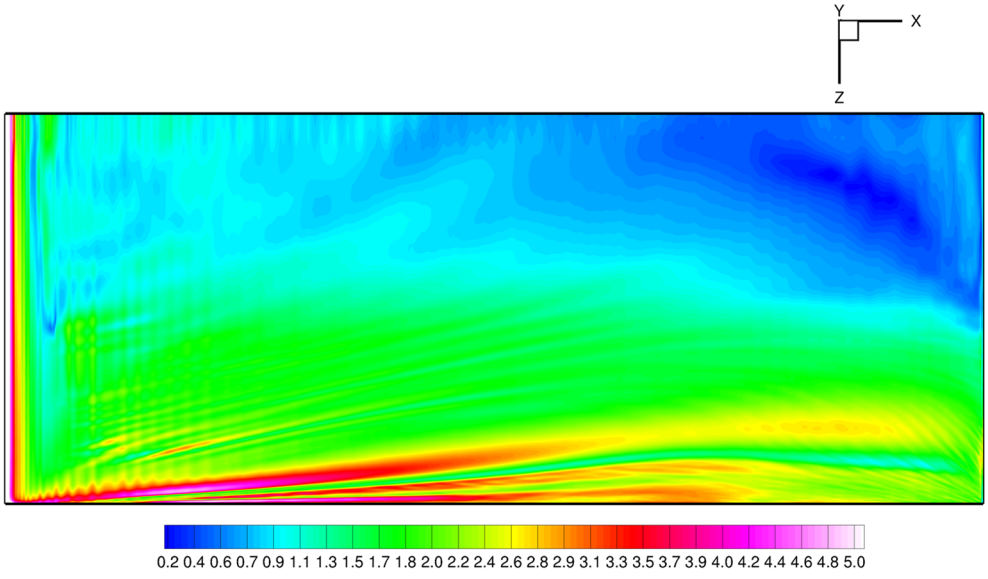

a) Upper surface

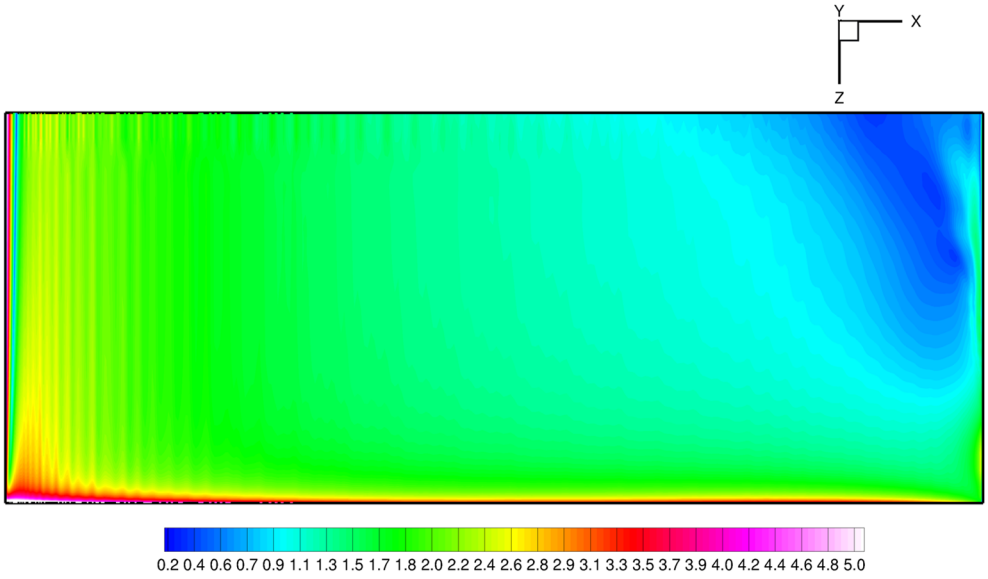

b) Lower surface

Fig. 6 Wall-normal grid resolution in terms of wall units on the wing surface near the tip.

simulation Reynolds number to 1.8×10^6 within the tip region only, whereas we lower the Reynolds number to 0.5×10^6 over part of the wing away from the tip. The total number of grid points at which the governing equations are solved is equal to approximately 110 million. Of these 110 million grid points, approximately 75 million points are located in the wing-tip region. Given the relatively high Reynolds number to be simulated and the available computational resources, this is the best resolution we can currently afford. We pay particular attention to the grid stretching within the critical regions of the flow domain and avoid severe stretching to ensure that the grid is smooth enough for the high-order simulation method. The grid over the wing geometry away from the tip is relatively coarser; thus, we artificially lower the Reynolds number to 0.5×10^6 in that region to avoid numerical instability problems. Nevertheless, the flow over the wing away from the tip is basically two-dimensional and relatively insensitive to Reynolds number. Thus, artificially lowering the Reynolds number in the region away from the tip is not expected to have adverse effects in the tip region.

The computational domain exactly models the wing geometry and the wind-tunnel walls. Both the tunnel width and height are equal to $5c$. The vertical distance between the quarter-chord axis of the wing geometry and the upper or lower tunnel walls is $2.5c$. We apply viscous-wall conditions only on the wing surface. For the temperature boundary condition, viscous walls are treated as isothermal walls. Tunnel walls are treated as inviscid walls, as the boundary layers forming on the tunnels walls are of no particular interest in this study. Multiblock and overset grids are used to discretize the computational domain.

We make use of overset grids to avoid grid-point singularities and control the grid density in various regions of the computational domain. In the computational grid, the inlet plane of the wind tunnel is set to be $2.5c$ away from the quarter-chord axis of the wing. The quarter-chord axis location is at $x/c = 0$. The outflow plane of the wind tunnel is located at $x/c = 4.07$. For the wind tunnel, characteristic-type inflow boundary conditions are applied on the inlet plane, and characteristic-type outflow boundary conditions are

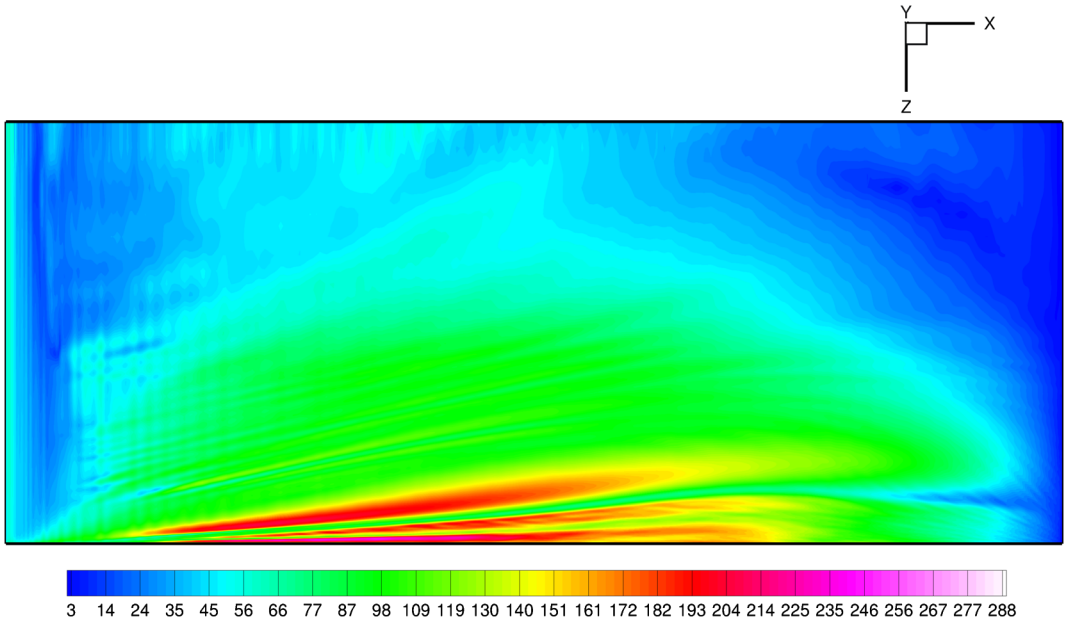

a) Upper surface

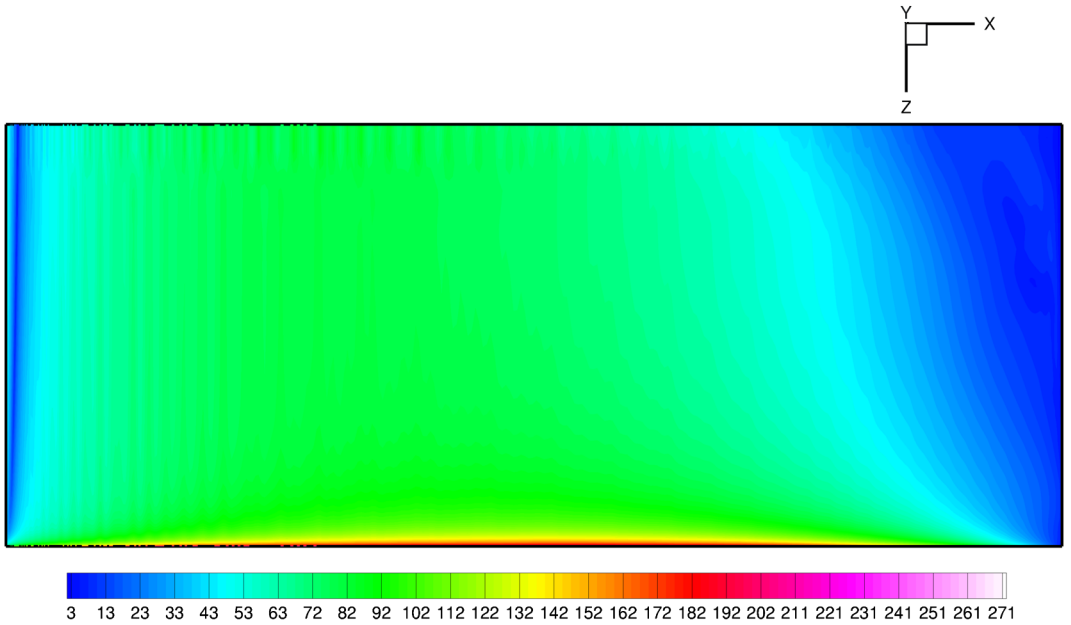

b) Lower surface

Fig. 7 Streamwise grid resolution in terms of wall units on the wing surface near the tip.

applied on the exit boundary. As mentioned earlier, all wind-tunnel walls are treated as inviscid walls.

The tip side region is discretized using overset grids to avoid the grid-point singularity problem near the leading and trailing edges. See Fig. 2 for the details of how the wing and tip surfaces are discretized. Figures 3 and 4 show the details of the overset grids on the tip side-edge surface, near the leading and trailing edge of the blunt tip, respectively. If one attempts to mesh the tip side surface by a single grid, then the issue of grid-point singularity arises. The singularity results from multiple grid lines converging into a single grid point. This is the same type of grid singularity problem that happens at the center of a circular domain when it is meshed using a cylindrical grid. The grid-point singularity happens near the leading and trailing edges of the side surface. The grid-point singularity problem is avoided by the use of two overset grids on the tip side surface, as shown in these figures. The tip side-surface grid shown in these figures covers most of the tip side-edge surface, and the tip side-patch grid covers the thin region around the tip side-edge chord line.

The wind-tunnel geometry is discretized using a box grid. The other grids that are generated around the wing geometry are embedded within this box grid. The overset grids communicate via high-order explicit interpolation. The overset grids that are used to discretize the computational domain are partitioned into 712 blocks total. The blocks are distributed to 712 processors. All blocks are approximately equal in size. This ensures a good load balance among the processors during the course of parallel computations.

Implicit time-stepping is used for the simulations. A nondimensional computational time step of $\Delta t u_\infty / c = 1 \times 10^{-4}$ is used in the computations. With this time step, it takes 10,000 time steps for a particle traveling at the freestream velocity u_∞ to travel one chord length. The nondimensional chord-flow time based on the freestream velocity is one time unit.

The first simulation reported in this paper, to be called simulation A, is performed as an ILES with no explicit SGS model. To reiterate, the spatial filter implemented in the flow solver for numerical stability is treated as an implicit SGS model. The other two

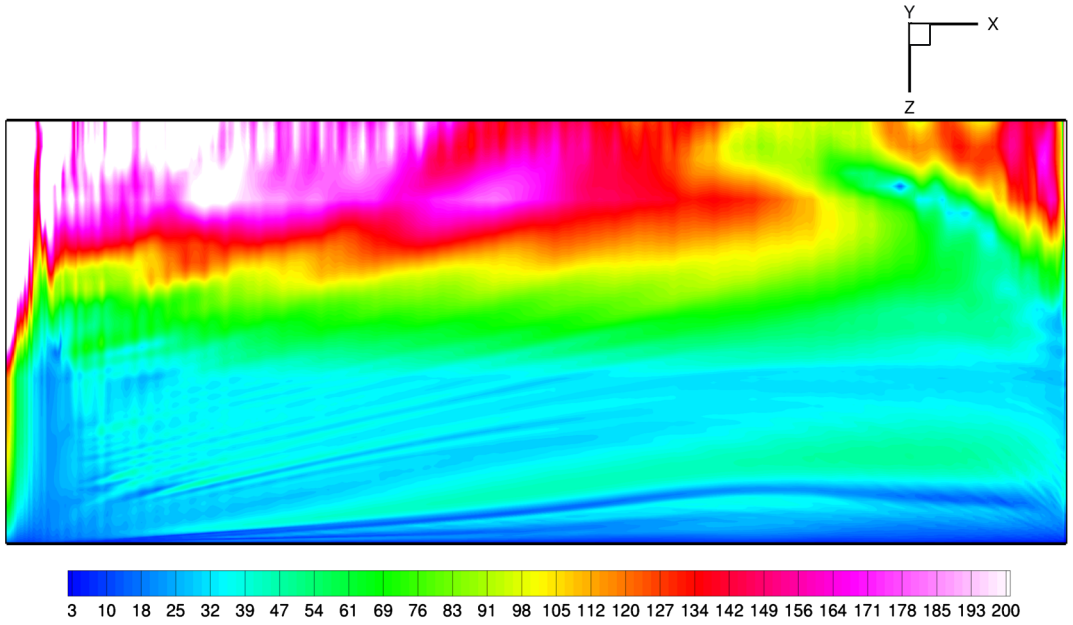

a) Upper surface

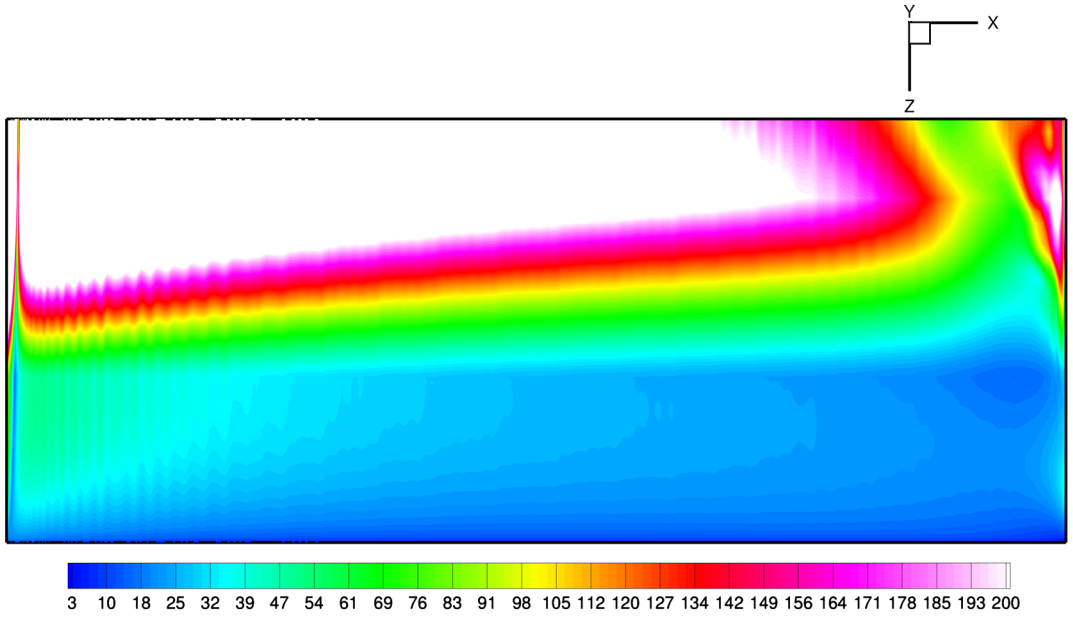

b) Lower surface

Fig. 8 Spanwise grid resolution in terms of wall units on the wing surface near the tip.

simulations are performed using the dynamic mixed model and the selective mixed-scale model and shall be called simulations B and C, respectively. The statistical sample size gathered in the simulations correspond to about five chord-flow times. This is the length of the time history of the unsteady data that are used for computing the flow statistics and the surface-pressure fluctuation spectra. Because of limited computational resources, this statistical sample size is a bit small; however, it is still large enough to make meaningful comparisons with experimental data. It was observed that the mean flow statistics of interest and mean surface pressures had converged sufficiently over this sampling period.

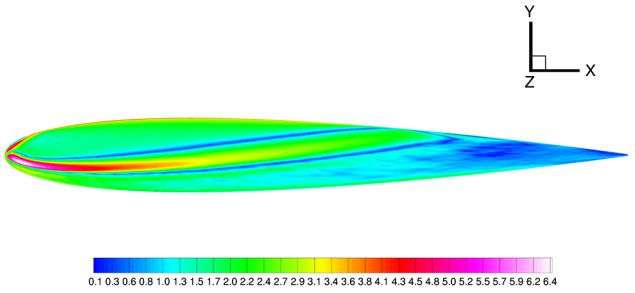

a) Wall-normal grid resolution in terms of wall units

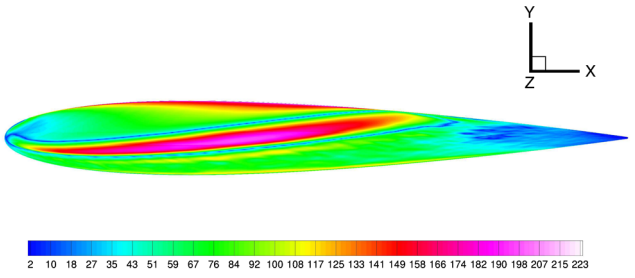

b) Streamwiselike grid resolution in terms of wall units

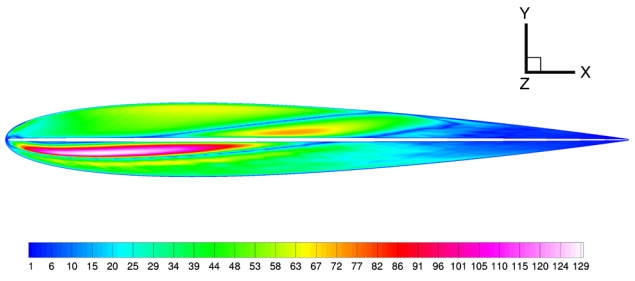

c) Spanwiselike grid resolution in terms of wall units

Fig. 9 Grid resolutions in wall units on the tip side-edge surface.

B. Simulation Results and Comparison with Experiment

The blunt tip geometry gives rise to the formation of two vortices, as seen in Fig. 5. The primary vortex forms over the upper surface of the wing, and the secondary vortex forms off of the side edge. The streamlines (from simulation A) depicted in Fig. 5 also show the merging of these two vortices around the wing trailing edge, which is a phenomenon that has been verified experimentally [10].

To examine how well the current computational grid can resolve the wing and tip surface near-wall regions at the given Reynolds number, we can examine the near-wall grid resolutions in wall units using the time-averaged boundary-layer data from the simulations. For example, the wall-normal grid resolution in wall units is defined as

$$\Delta W_n^+ = \frac{\Delta W_n}{c}\frac{u_\tau}{u_\infty} Re_c \tag{1}$$

where ΔW_n is the wall-normal distance and u_τ is the wall friction velocity. Time-averaged data from the ILES computation is used to determine the wall friction velocity in the above equation. The grid resolutions along the streamwise and spanwise directions in wall units can be defined similarly.

Figure 6 shows the wall-normal grid resolution on the wing surface near the tip, and Figs. 7 and 8 plot the wing surface streamwise and spanwise grid resolutions, respectively. All grid resolutions are expressed in terms of wall units. Similarly, Fig. 9 depicts the same

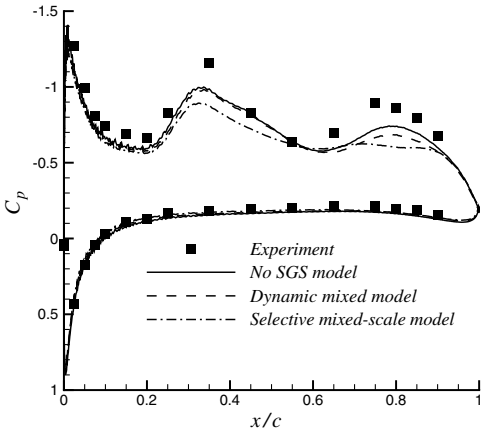

Fig. 11 Pressure-coefficient comparison on wing surface at $z/c = -0.0225$.

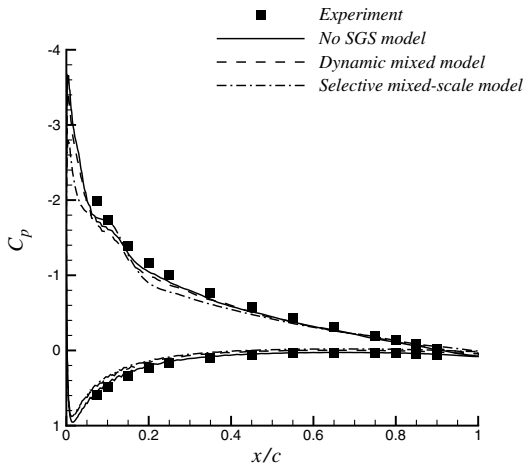

Fig. 10 Pressure-coefficient comparison on wing surface at $z/c = -1$.

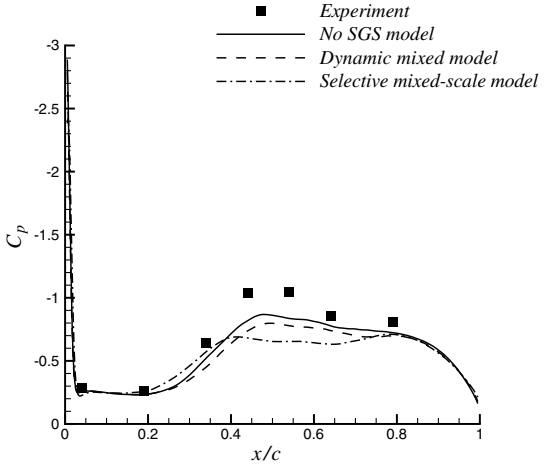

Fig. 12 Pressure-coefficient comparison on wing-tip side-edge chord line.

quantities on the tip side-edge surface. Note that for the wing surface, the streamwise and spanwise directions are well-defined and self-explanatory. For the tip side-edge surface grids, shown in Figs. 3 and 4, the streamwiselike direction should be thought of as the direction that runs along the chord, whereas the spanwiselike direction should be thought of as the other direction that runs transversely. Note that in Fig. 9c, the contours on the tip side-patch grid have not been plotted. As we use overset grids on the tip side edge, there is an inevitable jump in the grid size as we move from one grid to next. This jump in the grid size results in a noticeable discontinuity in the spanwiselike-direction grid-resolution contour plots, although the discontinuity is barely noticeable in the grid-resolution contours for the other two directions.

Looking at Fig. 6, we observe that on the wing upper and lower surfaces, the wall-normal grid spacing in wall units has a maximum value of around 10 over the leading edge, where the boundary layers are in a laminar state. Outside the leading-edge region, we see maximum values of around 5 or so near the tip. Additionally, on the upper surface, we see localized patches in which the highest wall-normal grid spacing values are around 5. These regions correspond to the areas in which the wing upper-surface boundary layers become thinner due to the interaction of the primary vortex with the upper wing surface. Outside these regions, the values are fairly low.

Looking at the streamwise grid resolution in wall units depicted in Fig. 7, we observe a trend similar to what we previously saw in Fig. 6. The only difference this time is that we do not see relatively high values near the leading edge, as the streamwise grid spacings on the wing leading edge are rather small. The highest values are seen near the tip. On the wing upper surface, we observe regions in which the streamwise grid resolution in wall units reaches values as high as 200 to 250. Outside these regions, the values are smaller than 100.

On the other hand, the contours plotted in Fig. 8 show that the spanwise grid resolution in wall units is smallest near the tip and becomes larger as we move away from the tip. The typical values seen very near the tip on the upper surface are around 20 and lower, whereas values around 30 to 50 are observed a bit further away from the tip. The values get much bigger as we move further away from the tip. The values seen in the near-tip region on the lower wing surface vary from 10 to about 50.

Figure 9 shows that the highest value of wall-normal grid resolution in wall units is around 6 on the tip side edge, whereas values as high as 225 are seen in the streamwiselike grid resolution in wall units and about 130 for the spanwiselike grid resolution in wall units. Note that the interaction of the secondary vortex with the tip side edge causes thinning of the boundary layers on this surface, thus resulting in such fairly high values.

From this analysis, it appears that the grid resolution in certain regions over the wing and tip side-edge surfaces is a bit coarse and it would be desirable to further refine the mesh in these regions to increase the resolution. As we are already using a significant number of grid points and we have access to limited computational resources, we did not attempt to further increase the grid resolution in this study.

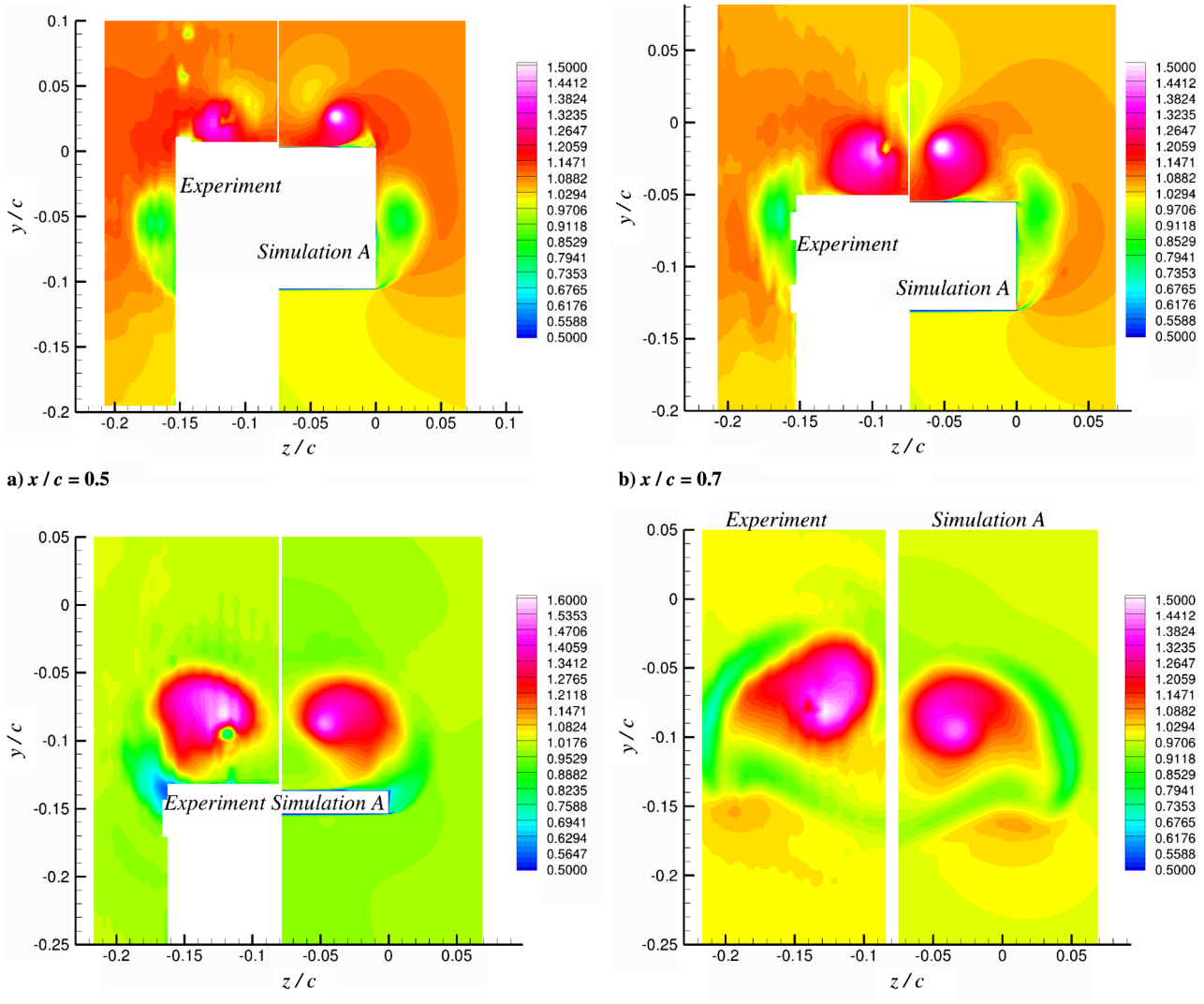

Fig. 13 Mean axial-velocity contour comparisons.

To make a quantitative comparison between the computational results and the experimental measurements, we first look at a comparison of the surface-pressure coefficient C_p distribution at various locations on the wing surface. Figure 10 shows the comparison at one chord length away from the tip. The wing-tip location is at $z/c = 0$, where z is the spanwise coordinate. In the C_p figures, x denotes the distance along the chord line of the airfoil. The effect of the tip vortex on the C_p distribution is insignificant at $z/c = -1$. As mentioned earlier, the Reynolds number of the simulation is adjusted along the spanwise direction, and it is equal to 0.5×10^6 at this spanwise station. Since the flow away from the tip region is essentially two-dimensional, the Reynolds number is not expected to have an important effect on the surface C_p distributions away from the tip region, thus justifying the comparison of the simulation data with the experimental data at this spanwise location. At this spanwise location, we observe good agreement between the computations and the experiment on both the upper- and lower-surface C_p distributions. However, simulation C, which employs the selective mixed-scale model, produces some notable differences relative to the experiment near the leading edge of the wing upper surface. It is not clear what the source of this difference is, but perhaps the chosen values of several adjustable parameters needed for this model are responsible for the observed behavior near the upper wing surface leading edge.

The C_p distributions at the spanwise location at $z/c = -0.0225$ are plotted in Fig. 11. In this figure, we see that all computations predict the C_p distribution on the lower wing surface quite well. When we look at the C_p distribution on the upper surface, we see that simulations A and B give similar predictions for the first peak, whereas simulation C produces a somewhat weaker peak. However, the first peak predicted by simulations A and B is still weaker than the one seen in the experiment. This first peak in the upper-surface C_p distribution is caused by the primary vortex, which is forming over the upper wing surface. Flow visualization pictures from both the experiment and the computation show that after formation, the primary vortex initially moves away from the surface with increasing axial distance. The movement of the primary vortex away from the surface causes the absolute values of C_p to decrease. A local minimum of the absolute value of C_p is observed at around $x/c = 0.6$ on the suction side in both the experiment and the computations. Moreover, it was observed that close to the trailing edge the primary vortex comes closer to the surface because of the influence of the secondary vortex; thus, another suction peak is observed in the C_p distribution near the trailing edge at around $x/c = 0.75$. Looking at the C_p peak near the trailing edge, we see the differences in the predictions of different SGS models. The best prediction is given by the ILES approach. The secondary peak gets progressively weaker with the other two explicit SGS models. The poorest prediction of the secondary peak is given by the selective mixed-scale model.

Figure 12 plots the surface C_p distribution along the chord line on the tip side edge. We see differences between the simulations and the experiment in the region where $0.4 < x/c < 0.7$. The experiment clearly shows a peak at around $x/c = 0.5$. In the experiment, it was observed that this is the location at which the secondary vortex forming off of the side edge crosses the tip side-edge chord line. We again see that the best agreement with the experiment is obtained by

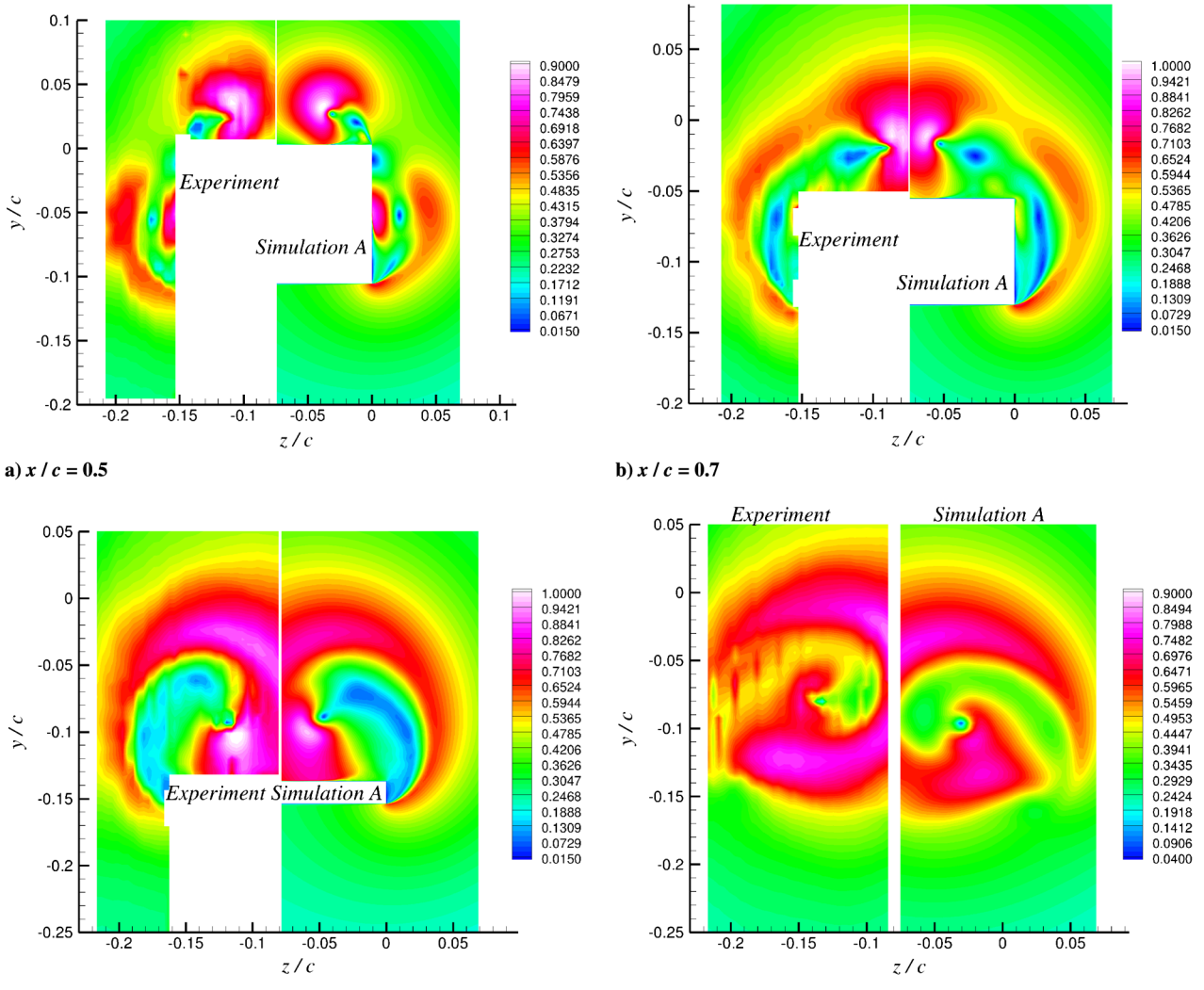

a) $x/c = 0.5$ **b) $x/c = 0.7$**

c) $x/c = 0.95$ **d) $x/c = 1.1$**

Fig. 14 Mean crossflow-velocity contour comparisons.

the ILES. The prediction of the dynamic mixed model is close to that of the ILES. The prediction of the selective mixed-scale model is again the poorest.

The explicit SGS models we tested include an eddy-viscosity term to model the dissipation effects of the unresolved length scales. The ILES approach has zero eddy-viscosity. Since the dynamic mixed model is a combination of the scale-similarity model and the dynamic Smagorinsky model, the magnitude of the eddy-viscosity of this model is smaller than that in the selective mixed-scale model. Thus, from the comparisons so far, it appears that the increasing magnitude of the eddy-viscosity in the SGS model adversely affects the surface C_p distributions around the tip region. Moreover, the selective mixed-scale model, which provides the poorest surface C_p predictions, contains several model parameters that need to be carefully chosen. The default parameter values we have chosen for this model are probably not the optimal values for the tip vortex problem.

To see the vortex structures in more detail, we will now make side-by-side comparisons of the experimental PIV measurements and simulation A results. Since the surface C_p distribution is directly tied to the mean flow of the tip vortex structure, and the ILES provided the best agreement with the experiment for C_p distributions, we use the ILES (simulation A) results to make comparisons with the experiment. In the following comparisons between the experiment and simulation A results, the data on the left two-dimensional plane denote the experimental measurements, and the data on the right plane denote the simulation results. For the sake of easier comparison, the experimental data planes are mirrored along the z direction. In these comparisons, the left boundary of the computational data plane and the right boundary of the experimental data plane coincide on the same physical z plane. The z/c values on the horizontal axes of these figures are only valid for the simulation data. To enable side-by-side comparison of the simulation data with the experiment, the experimental data has been mirrored and shifted along the horizontal axis. Thus, the z/c values on the horizontal axis do not denote the actual spanwise location of the experimental data. It should also be noted here that the experimental plots contain blank (or white) regions in which the quality of the data was rather poor; thus, those regions are omitted. Moreover, experimental PIV measurements are not available in the region very close to the wing surface. Thus, the near-wall regions in the experimental data are blank as well.

Figure 13 plots the mean axial-velocity contours on the four PIV planes, and Fig. 14 shows the mean crossflow-velocity contours on the same planes. The crossflow velocity is the magnitude of the velocity vector that is composed of the mean vertical and mean spanwise velocities. Figure 15 depicts the streamlines superimposed on the mean axial-velocity contour plots. The streamlines are constructed using the mean vertical and spanwise components of velocity. The PIV planes are perpendicular to the freestream direction. For these comparisons, x denotes the distance measured along the chord line, with $x/c = 0$ corresponding to the leading edge. The x/c values of the four PIV planes are 0.5, 0.7, 0.95, and 1.1, respectively.

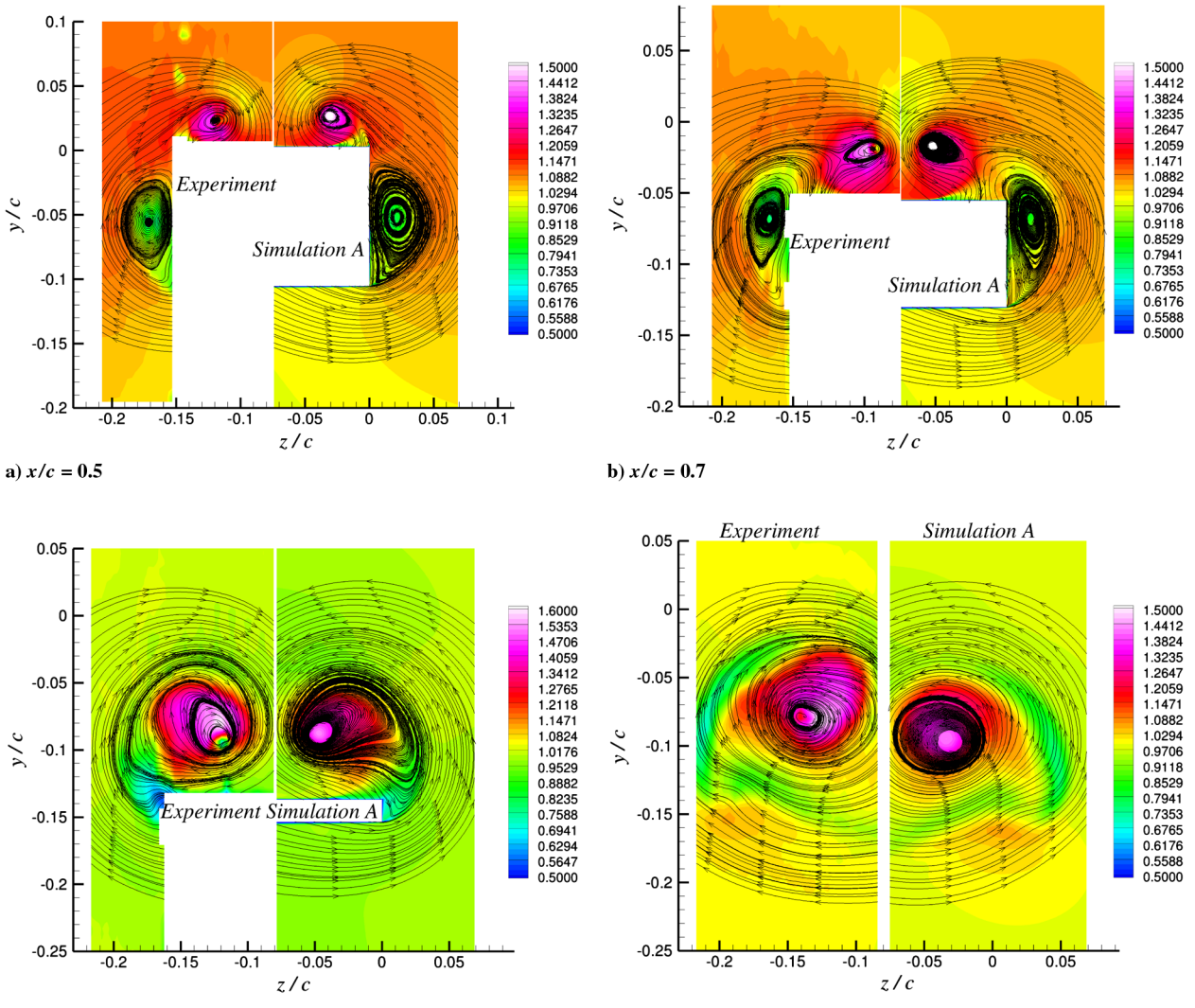

a) x/c = 0.5 **b) x/c = 0.7**

c) x/c = 0.95 **d) x/c = 1.1**

Fig. 15 Streamlines superimposed on mean axial-velocity contours.

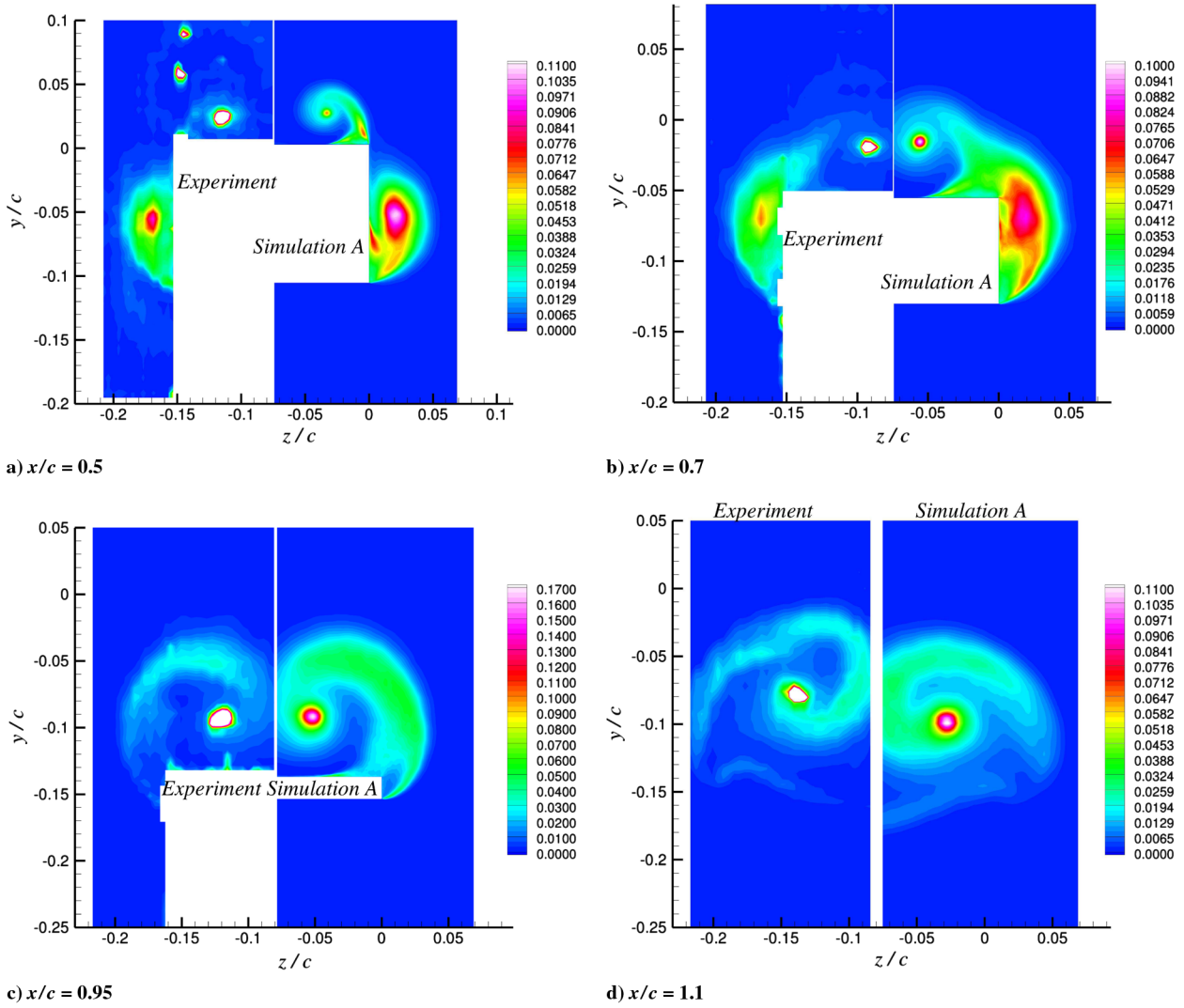

Fig. 16 Turbulent-kinetic-energy contour comparisons.

Looking through these figures, we notice good overall similarity between the experiment and simulation A. The initial formation of the primary and secondary vortices is clearly evident in both the ILES and the experiment at $x/c = 0.5$. As confirmed by both the experiment and the ILES, the primary vortex has a jet-type core, meaning that the core axial velocity is greater than the freestream value. In contrast, the secondary vortex has a wake-type core, meaning that the core axial velocity is smaller than the freestream value.

Some differences between simulation A and the experiment are visible. For example, on the first and second PIV planes, the peak axial velocity in the core of the primary vortex is a bit higher in the simulation. Other than this difference, we observe good overall similarity in the axial-velocity contours on the first two PIV planes. Mean crossflow velocity and streamline comparison figures for the first two PIV planes also demonstrate a good level of similarity between the experiment and simulation A. The peak crossflow velocities occur near the core of the primary vortex. We start to see more noticeable differences on the third and fourth PIV planes. By the third PIV plane, the primary and the secondary vortices have merged together in both the ILES and the experiment. The peak crossflow velocities on the third and fourth PIV planes are slightly larger in the experiment. On the fourth plane, we also see that the vertical position of the merged vortex core in the simulation is located a bit lower than the experimental vortex.

Figure 16 plots the turbulent-kinetic-energy contour comparison. As can be seen from the figures, despite some differences, the agreement between simulation A and the experiment is still satisfactory. On the first PIV plane, we see significant turbulent kinetic energy inside and surrounding the core of the secondary vortex forming of the side edge. The region containing high levels of turbulent kinetic energy within the core of the secondary vortex appears larger in the simulation. We also see some turbulent kinetic energy in the separated boundary layers on the upper surface of the wing that are getting wrapped into the primary vortex. On the second PIV plane, we see that much of the turbulent kinetic energy resides within the secondary vortex in both the experiment and simulation A. However, in simulation A, we again observe that the region containing high levels of turbulent kinetic energy inside and around the secondary vortex core is larger. We also see that there is significant turbulent kinetic energy in the upper-wing-surface detached boundary layers in the simulation, whereas we do not really see that in the experiment. Part of the separated boundary-layer flow over the upper wing surface is getting absorbed into the secondary vortex, and the remainder is wrapped into the primary vortex. Looking at the third and fourth PIV planes, we again see a fair amount of similarity. The turbulent-kinetic-energy contours on these planes express a spiral-shaped pattern in both the experiment and the simulation. The turbulent kinetic energy is spread out over a wider area in the simulation. On the third plane, we again see significant turbulent kinetic energy in the wing boundary layers that are separating off the surface and getting absorbed into the merged vortex. However, the experimental measurements do not appear to show a similar phenomenon.

The comparison of nondimensional mean axial-vorticity-magnitude contours, depicted in Fig. 17, once again demonstrates

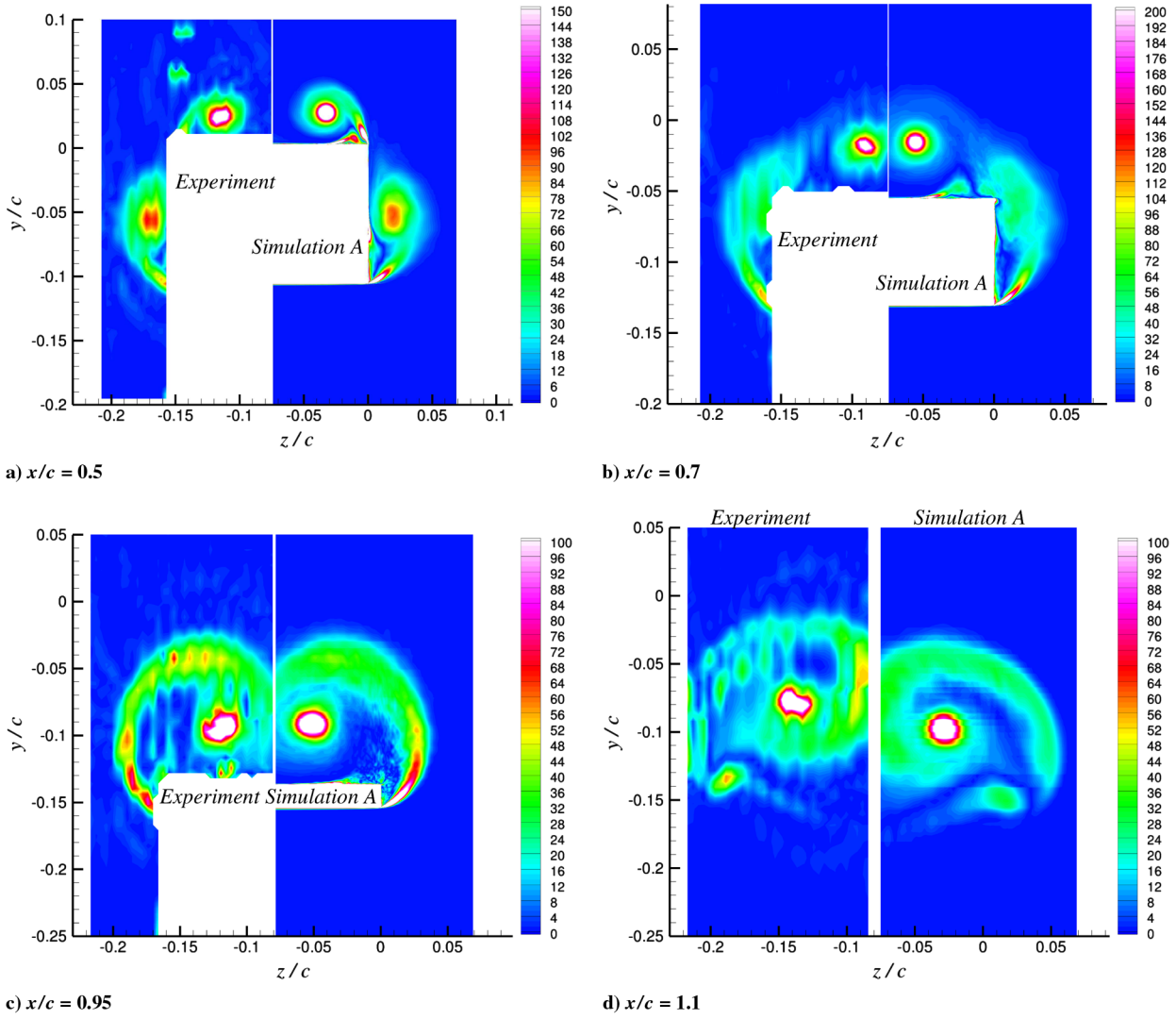

Fig. 17 Mean axial-vorticity-magnitude contour comparisons.

good overall similarity between the experiment and ILES. On the first PIV plane, both the ILES and the experiment show that the axial vorticity within the core of the primary vortex is significantly higher than that seen in the core of the secondary vortex. We also observe relatively high levels of axial vorticity within the detached boundary layers that are getting wrapped into the vortices in the ILES. The ILES also shows much higher levels of axial vorticity in the very near-wall regions, due to the presence of large boundary-layer velocity gradients there. The observations made on the second PIV plane comparison are similar to those on the first PIV plane comparison. By the third PIV plane, as previously discussed, the two vortices fully merge together. Other than the very near-wall region, we observe the peak levels of the axial vorticity within the core of the merged vortex and in the detached boundary layer separating off the lower wing surface. On the last PIV plane, the contours once again conform to a spiral pattern and, as expected, the core of the merged vortex has the highest levels of axial vorticity.

Finally, we take a look at the surface C_p spectra obtained from the ILES and their comparison with the experiment. For the sake of brevity, we will only show the spectra from simulation A. Although

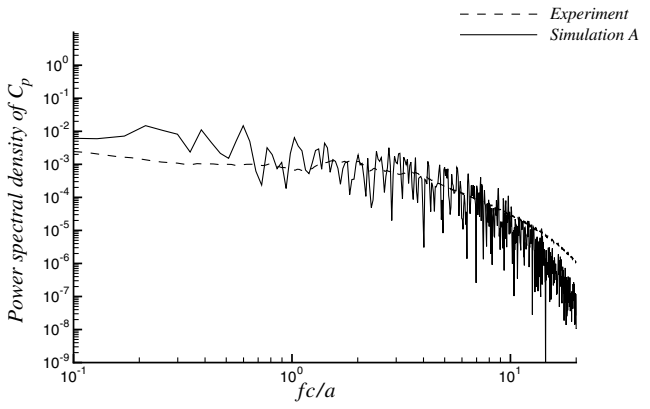

Fig. 18 Power spectral density of C_p on the tip side edge at $x/c = 0.35$.

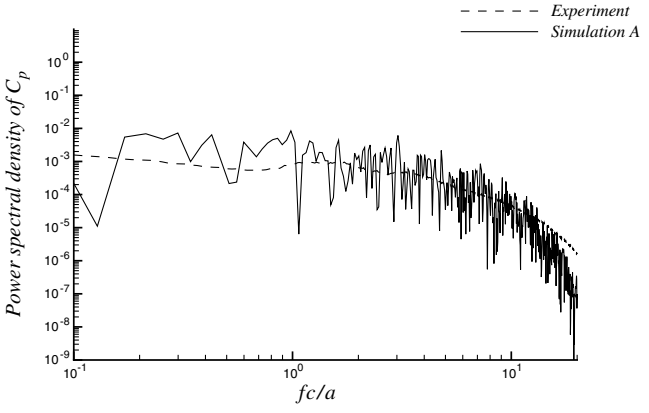

Fig. 19 Power spectral density of C_p on the tip side edge at $x/c = 0.45$.

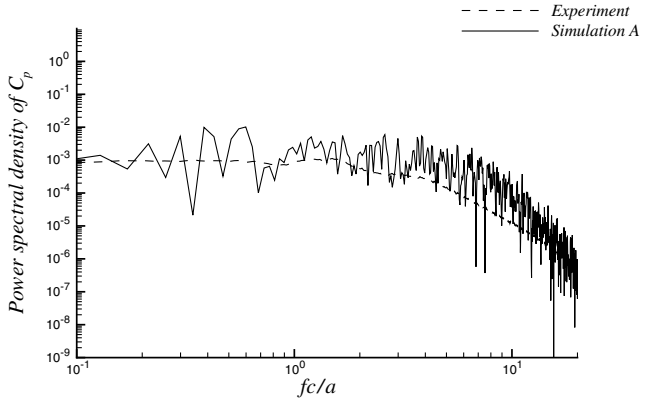

Fig. 20 Power spectral density of C_p on the tip side edge at $x/c = 0.55$.

not shown here, we compared simulation A spectra with those from simulations B and C, and neither of the other calculations provided spectra results that compared better with the experiment than did simulation A spectra. The tip side-edge spectra taken at $x/c = 0.35$, 0.45, 0.55, and 0.65 are plotted in Figs. 18–21, respectively. The spectra taken at $x/c = 0.65, 0.8$ on the wing upper surface are shown in Figs. 22 and 23, respectively. Here, x is the axial distance measured along the chord, starting from the leading edge. In these plots, the horizontal axis is the frequency nondimensionalized by the wing chord length c and the sound speed a. It should be noted that the simulation spectra display large wiggles from one frequency to the next, due to the limited sample size gathered in the simulation.

It is observed that at $x/c = 0.35$ and 0.45 on the tip side edge, the overall agreement of the ILES and the experiment is fairly good up to about $fc/a \approx 10$ or so. The ILES spectra display much less spectral

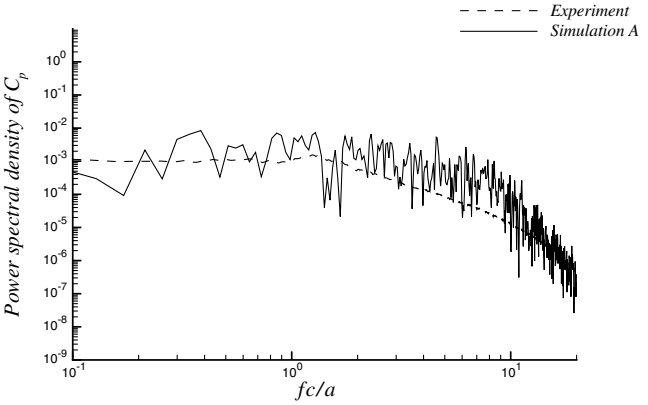

Fig. 21 Power spectral density of C_p on the tip side edge at $x/c = 0.65$.

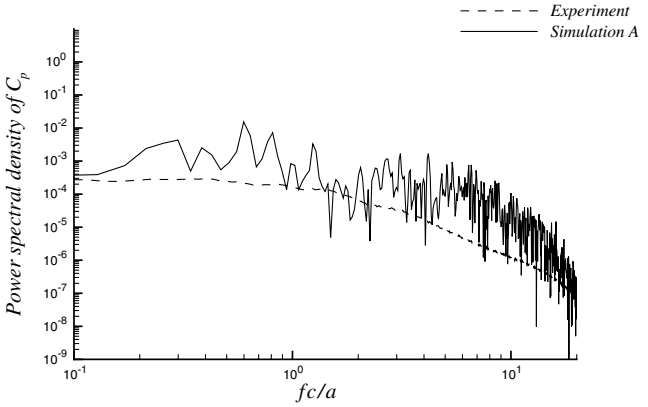

Fig. 22 Power spectral density of C_p on the wing upper surface at $x/c = 0.65$ and $z/c = -0.0125$.

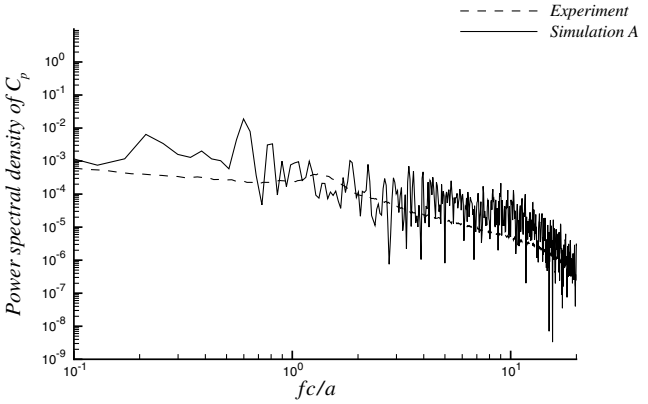

Fig. 23 Power spectral density of C_p on the wing upper surface at $x/c = 0.8$ and $z/c = -0.0125$.

energy in the higher frequencies. This could be due to the mesh resolution on the tip side-edge surface at these locations. At the remaining two comparison locations on the tip side edge, the overall agreement is still good, but this time we observe that the ILES spectra have somewhat higher spectral energy levels in the range from $fc/a \approx 3$ to ≈ 10. The comparisons at the two spectra locations on the wing upper surface tell a similar story. We see good overall agreement in the spectral shapes, whereas we observe a mismatch of spectral energy levels in certain regions of the frequency range. All in all, despite some of the observed differences, the general agreement between the ILES and experimental surface C_p spectra is found to be satisfactory. Note that previous comparisons of the surface C_p distributions and tip vortex mean flow structure showed some differences between the ILES and the experiment. Such differences in the mean tip vortex flow structure could likely be responsible for some of the differences seen in the surface C_p spectra comparisons.

IV. Conclusions

In this study, we have performed numerical simulations of vortex formation around a blunt tip geometry using several SGS models. A computational grid containing around 110 million points was used in the simulations. Multiblock and overset grids were used to exactly model the experimental setup and discretize the computational domain around the wing geometry. The first simulation was performed as an ILES, in which there was no explicit subgrid-scale model. The numerical dissipation provided by the filtering operation is treated as an implicit subgrid-scale model. Two explicit subgrid-scale models were also used in the LES to investigate whether they could further improve the results. Yet neither of the tested explicit subgrid-scale models provided results better than those of the ILES. The best agreement with the experiment is obtained by the ILES. As the surface-pressure fluctuations carry a footprint of the far-field noise, and the ILES spectra matched the experimental surface spectra the best, we expect that the ILES would produce the best agreement with the experiment for the far-field noise well. Unfortunately, there were no far-field noise measurements taken in the experiment; thus, it was not possible to make a comparison of the far-field noise predictions with the experiment. Although there were some differences observed between the ILES results and the experimental measurements, the overall agreement between the ILES and the experiment was found to be satisfactory. Limitations on affordable grid resolution and uncertainties in the experimental measurements are believed to be the primary causes for the observed differences. Nevertheless, despite some of these issues, it is shown that the current numerical simulations can produce reliable results for a fairly-high-Reynolds-number test case. Now that the quality of the simulation data has been established, further work may use the data available from these calculations to look deeper into the physics of the tip vortex problem.

Acknowledgments

This research is sponsored by NASA Langley Research Center. This work is also partially supported by the National Center for Supercomputing Applications (NCSA), Louisiana Optical Network Initiative (LONI), and Texas Advanced Computing Center (TACC) under the TeraGrid grant MCA06N043. Computations used the NCSA Intel 64 Linux Cluster Abe, LONI Intel Linux Cluster Queen Bee, and TACC Sun Constellation Linux Cluster Ranger. We acknowledge useful discussions with David Lockard, who serves as the NASA Technical Monitor for this project. We are grateful to Taro Imamura for making the experimental measurements available to us.

References

[1] Dacles-Mariani, J., Zilliac, G. G., Chow, J. S., and Bradshaw, P., "Numerical/Experimental Study of a Wingtip Vortex in the Near Field," *AIAA Journal*, Vol. 33, No. 9, Sept. 1995, pp. 1561–1568. doi:10.2514/3.12826

[2] Dacles-Mariani, J., Kwak, D., and Zilliac, G., "On Numerical Errors and Turbulence Modeling in Tip Vortex Flow Prediction," *International Journal for Numerical Methods in Fluids*, Vol. 30, No. 1, May 1999, pp. 65–82. doi:10.1002/(SICI)1097-0363(19990515)30:1<65::AID-FLD839>3.0.CO;2-Y

[3] Kim, S.-E., and Rhee, S. H., "Prediction of Tip-Vortex Flow Past a Finite Wing," AIAA Paper 2005-0058, Jan. 2005.

[4] Takallu, M. A., and Laflin, K. R., "Reynolds-Averaged Navier–Stokes Simulations of Two Partial-Span Flap Wing Experiments," AIAA Paper 98-0701, 1998.

[5] Khorrami, M. R., Singer, B. A., and Radeztsky, R. H., "Reynolds Averaged Navier–Stokes Computations of a Flap Side-Edge Flow Field," AIAA Paper 98-0768, 1998.

[6] Fleig, O., Iida, M., and Arakawa, C., "Wind Turbine Blade Tip Flow and Noise Prediction by Large-Eddy Simulation," *Journal of Solar Energy Engineering*, Vol. 126, No. 4, Nov. 2004, pp. 1017–1024. doi:10.1115/1.1800551

[7] Fleig, O., Iida, M., and Arakawa, C., "Wind Turbine Flow and Noise Prediction by Large Eddy Simulation," AIAA Paper 2005-1188, Jan. 2005.

[8] Cai, J., Deng, S., Xie, P., and Liu, C., "High-Order LES for Wing Tip Vortex in the Near Field," AIAA Paper 2005-1125, Jan. 2005.

[9] Ghias, R., Mittal, R., Dong, H., and Lund, T., "Study of Tip-Vortex Formation Using Large-Eddy Simulation," AIAA Paper 2005-1280, Jan. 2005.

[10] Imamura, T., Enomoto, S., Kato, H., Yokokawa, Y., and Yamamoto, K., "Numerical Simulation of NACA0012 Wingtip Flow Leading to Noise Generation," AIAA Paper 2005-2864, 2005.

[11] Imamura, T., Enomoto, S., and Yamamoto, K., "Noise Generation Around NACA0012 Wingtip Using Large- Eddy-Simulation," *25th Congress of the International Council of the Aeronautical Sciences (ICAS)*, Hamburg, Germany, 2006.

[12] Uzun, A., Hussaini, M. Y., and Streett, C. L., "Large-Eddy Simulation of a Wing Tip Vortex on Overset Grids," *AIAA Journal*, Vol. 44, No. 6, 2006, pp. 1229–1242. doi:10.2514/1.17999

[13] Visbal, M. R., and Gaitonde, D. V., "Very High-order Spatially Implicit Schemes for Computational Acoustics on Curvilinear Meshes," *Journal of Computational Acoustics*, Vol. 9, No. 4, 2001, pp. 1259–1286.

[14] Ashcroft, G., and Zhang, X., "Optimized Prefactored Compact Schemes," *Journal of Computational Physics*, Vol. 190, No. 2, 2003, pp. 459–477. doi:10.1016/S0021-9991(03)00293-6

[15] Uzun, A., and Hussaini, M. Y., "Investigation of High Frequency Noise Generation in the Near-Nozzle Region of a Jet Using Large Eddy Simulation," *Theoretical and Computational Fluid Dynamics*, Vol. 21, No. 4, 2007, pp. 291–321. doi:10.1007/s00162-007-0048-z

[16] Uzun, A., and Hussaini, M. Y., "Simulation of Noise Generation in Near-Nozzle Region of a Chevron Nozzle Jet," *AIAA Journal*, Vol. 47, No. 8, 2009, pp. 1793–1810. doi:10.2514/1.36659

[17] Visbal, M. R., and Rizzetta, D. P., "Large-Eddy Simulation on Curvilinear Grids Using Compact Differencing and Filtering Schemes," *Journal of Fluids Engineering*, Vol. 124, No. 4, Dec. 2002, pp. 836–847. doi:10.1115/1.1517564

[18] Visbal, M. R., Morgan, P. E., and Rizzetta, D. P., "An Implicit LES Approach Based on High-Order Compact Differencing and Filtering Schemes," AIAA Paper 2003-4098, June 2003.

[19] Sherer, S. E., and Visbal, M. R., "Implicit Large Eddy Simulations Using a High-Order Overset Grid Solver," AIAA Paper 2004-2530, July 2004.

[20] Zang, Y., Street, R. L., and Koseff, J. R., "A Dynamic Mixed Subgrid-Scale Model and Its Application to Turbulent Recirculating Flows," *Physics of Fluids A*, Vol. 5, No. 12, Dec. 1993, pp. 3186–3196. doi:10.1063/1.858675

[21] Salvetti, M. V., and Banerjee, S., "A Priori Tests of a New Dynamic Subgrid-Scale Model for Finite-Difference Large-Eddy Simulations," *Physics of Fluids*, Vol. 7, No. 11, Nov. 1995, pp. 2831–2847. doi:10.1063/1.868779

[22] Bardina, J., Ferziger, J. H., and Reynolds, W. C., "Improved Subgrid Scale Models for Large Eddy Simulation," AIAA Paper 80-1357, July 1980.

[23] Meneveau, C., and Katz, J., "Scale-Invariance and Turbulence Models for Large-Eddy Simulation," *Annual Review of Fluid Mechanics*, Vol. 32, 2000, pp. 1–32. doi:10.1146/annurev.fluid.32.1.1

[24] Sagaut, P., and Grohens, R., "Discrete Filters for Large Eddy Simulation," *International Journal for Numerical Methods in Fluids*, Vol. 31, No. 8, Dec. 1999, pp. 1195–1220. doi:10.1002/(SICI)1097-0363(19991230)31:8<1195::AID-FLD914>3.0.CO;2-H

[25] Lenormand, E., Sagaut, P., and Phuoc, L. T., "Large Eddy Simulation of Subsonic and Supersonic Channel Flow at Moderate Reynolds Number," *International Journal for Numerical Methods in Fluids*, Vol. 32, No. 4, Feb. 2000, pp. 369–406. doi:10.1002/(SICI)1097-0363(20000229)32:4<369::AID-FLD943>3.0.CO;2-6

[26] Lenormand, E., Sagaut, P., Phuoc, L. T., and Comte, P., "Subgrid-Scale Models for Large-Eddy Simulations of Compressible Wall Bounded Flows," *AIAA Journal*, Vol. 38, No. 8, Aug. 2000, pp. 1340–1350. doi:10.2514/2.1133

P. Givi
Associate Editor